

Automatic Diabetic Retinopathy grading system using U-net and ANN

Peush Paul S^{1,*}, Prof. J M Aravind², Dr. V Suresh³

¹ ME Student, Department of ECE, Mar Ephraem College of Engineering and Technology, Elavuvilai

² Professor, Department of ECE, Mar Ephraem College of Engineering and Technology, Elavuvilai

³ Head of Department, Department of ECE, Mar Ephraem College of Engineering and Technology, Elavuvilai

Abstract— Multi-label classification (MLC) is considered an essential research subject in the computer vision field, principally in medical image analysis. For this merit, we derive benefits from MLC to diagnose multiple grades of diabetic retinopathy (DR) from various colored fundus images, especially from multi-label (ML) datasets. Therefore, ophthalmologists can detect early signs of DR as well as various grades to initiate appropriate treatment and avoid DR complications. In this paper, we propose a comprehensive ML computer-aided diagnosis (CAD) system based on deep learning technique. First, we eliminate noise, enhance quality, and standardize the sizes of the retinal images. Second, we differentiated between the healthy and DR cases by calculating the gray level run length matrix average in four different directions. The system automatically extracts the four changes: exudates, microaneurysms, hemorrhages, and blood vessels by utilizing a deep learning technique (U-Net). Furthermore, multi-oriented gradient weighting is combined with U-Net to achieve accurate segmentation. Next, we extract six features, which are the gray level co-occurrence matrix, areas of the four segmenting pathology variations, and the bifurcation points count of the blood vessels. Finally, the resulting features were afforded to an Artificial Neural Network (ANN) based on a classifier chain to differentiate the various DR grades. We utilized eight benchmark datasets (four of them are considered ML) and six different performance evaluation metrics to evaluate the proposed system's performance. It achieved 95.1%, 91.9%, 86.1%, 86.8%, 84.7%, 86.2% for accuracy, area under the curve, sensitivity, specificity, positive predictive value, and dice similarity coefficient, respectively. The experiments show encouraging results as compared with other systems.

Keywords—: *Multi-label computer-aided diagnosis (ML-CAD), multi-label classification (MLC), deep learning (DL), U-Net, diabetic retinopathy (DR).*

I. INTRODUCTION

Diabetic Retinopathy (DR) is an eye abnormality caused by long term diabetes and it is one of the causes of vision impairment. DR is the most common cause of blindness before the age of 50 years [1, 2]. DR is a progressive disease but the main issue with the disease is that a patient with DR has almost no signs of vision impairment at the initial stages of the disease. The severity of DR is determined by the number and types of lesions present on the surface of the retina.

The human retina consists of different components, such as blood vessels, the fovea, the macula, and the optic disc (OD). DR is broadly divided into two stages: non-proliferative DR (NPDR) and proliferative DR (PDR). NPDR occurs when the blood vessels get damaged inside the retina and leak fluid onto the retina [3], causing the retina to become wet and swollen. In NPDR, different signs of retinopathy can exist, such as microaneurysms (MAs), haemorrhages (HMs), exudates (hard and soft) (EXs), and inter-retinal microvascular abnormalities (IRMA) [4]. PDR is an advanced stage of DR in which new abnormal blood vessels start growing in different regions of the retina and may lead to total blindness. In this paper, we mainly consider only those NPDR lesions which are MAs, HMs, or EXs.

MAs are the first sign of DR to be visible to an ophthalmologist; they occur due to leakage from tiny blood vessels of the retina. They are of smaller size, are circular in shape, and are red in color. HMs occur when the walls of MAs get ruptured. Dot haemorrhages are like bright red dots, and blot haemorrhages are larger red lesions [2]. When the leakage of blood contains lipids and proteins, it creates yellow spots on the retina known as EXs. They cause complete blindness if the accumulation of the lipid is near or on the macula. MAs and HMs are referred to as dark lesions and EXs as bright lesions [4]. The ophthalmologists normally grade NPDR into three categories: i.e., mild, moderate and severe, depending on the location and occurrence of the lesions [4]. Fig. 1 shows a

healthy retina along with its main components. It also shows examples from different categories of NPDR.

The proposed framework is developed based on four security necessities:

- To design a ML-CAD system, visualizes the different pathological changes and diagnoses the DR grades for the ophthalmologists
- Introduce a deep learning technique for segmenting the four pathological variations (BV, EX, MA, and HM)
- A new candidate extraction technique is employed which extracts the potential DR candidates

- Utilizing ANN classifier provides the flexibility to future grading based on other lesion detection

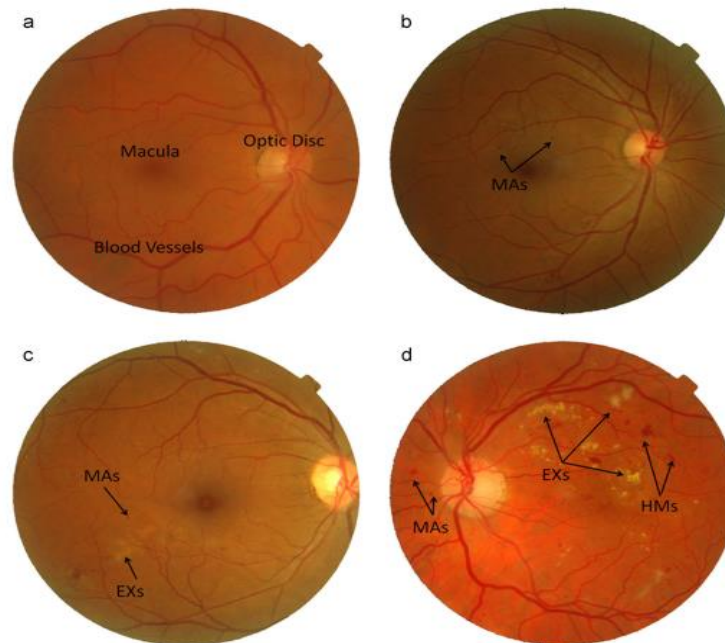


Fig. 1. Human retina and NPDR stages: (a) normal retina along with main components, (b) mild NPDR, (c) moderate NPDR, and (d) severe NPDR

2. LITERATURE SURVEY

There are several approaches for the automatic detection of MAs in color retinal images. These approaches can be generally classified into three groups which use morphological-based approaches, template matching, or supervised learning or some combination of each [9], [11], [22]–[36]. Similarly, some of these works aim for the automatic detection of DR [27], [28], [35], [36].

In [8] and [37] morphological algorithms are used to increase the detection accuracy for MAs. Although this type of analysis is typically fast and easy to apply, its simplicity can result in poor segmentation [30]. Morphological operations

such as closing [9], and the top-hat transformation [11] have been used for the detection of MAs, tuned to their relatively uniform circular shape and limited size range. Wang et al. [25] used a dark object filtering process to locate candidates. Next, singular spectrum analysis was used to decompose cross-sectional profiles of extracted candidates. Finally, a kNN classifier and a set of statistical features of profiles were employed to distinguish the MAs from nonMAs. However, besides the above issue, most of the mathematical morphology methods mainly depend on the correct choice of structuring elements, and its benefits may be lost in tailoring their size and shape to match the range of MAs.

Another method utilizes template matching with multiscale Gaussian kernels [24], [26], [29] because MAs approximate to a Gaussian-like peak in all projections and the intensity distribution of MAs is matched to a Gaussian distribution [24]. Therefore, template matching-based MA detection approaches have been proposed that can significantly increase the accuracy of MA detection. Using this idea, Quellec et al. applied a wavelet transform method for MAs detection. In their approach, they detected the MAs using local template matching in the wavelet domain [24]. Zhang et al. [26] used a multi-scale correlation coefficient based approach based on a non-linear filter with five Gaussian kernels at various standard deviations to detect MA candidates. Ram et al.

Xu et al. [28] introduced a system for detecting only DR's presence/absence. They presented A CNN model with 10- CNN layers. After each two CNN layers, they inserted one max pooling (MP) layer then the FC layers. They utilized the SGD optimizer and the softmax classifier. They cared about the preprocessing by doing data augmentations, but they utilized a small dataset. Pratt et al. [29] presented a CNN model that included 10-layers of CNN, three FC layers, and classification to five classes by the softmax classifier. They used the rectified linear unit (ReLU) as an activation function. Besides, they used batch normalization (BN) and used MP to occur after each CONV layer. Unlike [28], the authors ignored the preprocessing stage in their proposed system. In fact, noise affected their classification results. Moreover, it is necessary to utilize more than one dataset to achieve reality and robustness.

Butt et al. [30] built CNN models like [28] and [29], but the difference in their work was that they built three CNN modules based on RGB channels. They separated the RGB fundus images to R, G, and B and supplied each one in a distinct model. The authors concluded that the second model with the B channel gave better accuracy than the models with R and G channels. Li et al. [31] utilized fractional MP in CNN to detect five classes of DR. The authors processed the images by rescaling and clipping. They utilized an SVM classifier with a modified recognition rate. Although the authors built two CNN models with different layers to get different feature spaces and combine the best predictions by SVM classifier, they need sufficient and balanced groups of images, such as [29]. They failed to predict classes 3 and 4 accurately and hardly differentiated class 0 from class 1 in testing new data.

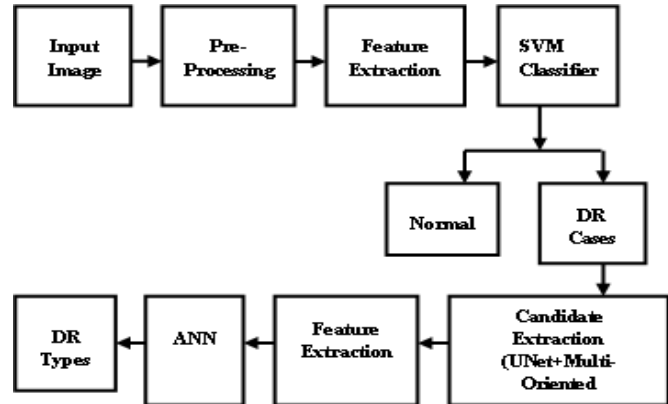


Fig 1 System Architecture

III SYSTEM OVERVIEW

The proposed ML-CAD system, which consists of eight phases. First, the preprocessing phase eliminates noise and enhances images. Second, the feature extraction phase is implemented to retrieve the entered fundus images' main characteristics. Third, the SVM classification phase uses the feature vector to classify the images into normal and DR cases. This phase provides only the DR cases to the next phases to reduce time, memory space, and effort. Fourth, make the post-processing phase, which contains three steps. First, resizing all the images and their ground truth (GTs) to be in a standard size of 512×512 and enable validation between the predicting and the segmenting images. Gradient weighting technique is used for the detection of small objects with weak boundaries and low contrast. Second, creating the mask for each image to be excluded in the segmentation. Third, to train the U-Net model on the three lesions GT's (MA, EX, and HM). The fifth phase in the proposed framework is the segmentation by utilizing the customized U-Net model. In sixth phase, performed the feature extraction on the ROIs. The resulting feature vector is fed to the classification, the seventh phase of the proposed framework. Utilized the ANN classifiers, to classify the other four DR grades. Finally, evaluated binary classification, segmentation, and final ANN performance by utilizing six various performance metrics.

IV PROPOSED SCHEMES

A. PREPROCESSING

This phase is crucial in any medical system as the medical images are characterized by artifacts, noise, and insufficient quality that vary from one modality to the other. In this respect, fundus images suffer from low contrast, illumination, and noise. Therefore, the proposed system

includes some steps in the preprocessing phase to enhance the quality and remove the noise. First, we apply the median filter to strip noise [33]. Then, we utilized HEBPDS [32] to enhance the contrast of the fundus images. At the end of the preprocessing phase, we extracted the green channel from the RGB enhanced image to use it in the feature extraction and the binary classification by GLRLM and SVM. Fig 2 shows the preprocessing phase result

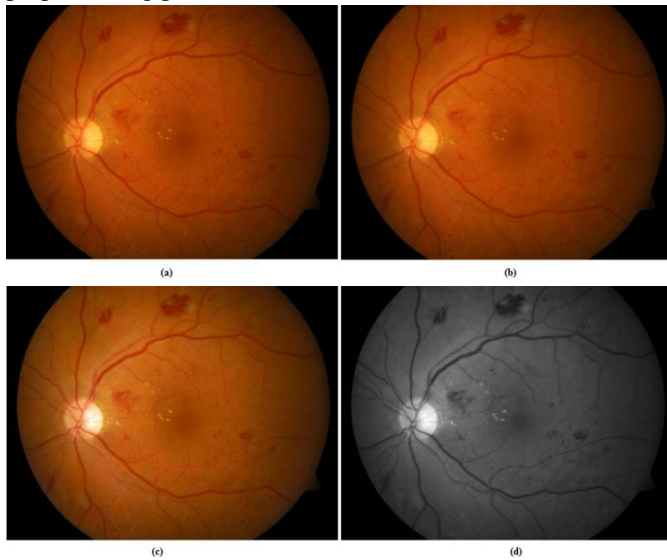


Fig 2 Preprocessing phase result: (a) Original Image (b) Denoising Image (c) Contrast Enhancement (d) Green Channel Image

B. GLRLM EXTRACTION

In the first extraction phase of the proposed framework, we utilized GLRLM to extract the features of the green channel of all processed images [34]. The resulting feature vector is used to differentiate normal and DR cases. To illustrate how the GLRLM works, we represented it by (gl, rl, θ) , where gl is the gray level, rl is the run length, and θ is the direction angle. It is a way of testing an image across a given direction to find the pixels with the same gray level values. Thus, it gives the homogeneous runs' size for each gray level. Many different GLRLM matrices can be computed for a single image as we utilized 11 matrices of them. Each matrix is calculated for each selected direction of the preprocessed image. Therefore, we calculated 11 GLRLM matrices in four different directions 0° , 45° , 90° , and 135° . We computed these 11 matrices' average in 4 directions to get a single averaged GLRLM matrix for each image. The main GLRLM construction for processed fundus images and the feature

vector steps' measurement is shown in two algorithms, which are found in [35]. GLRLM can be represented by Eq. 1.

$$GLRLM(\theta) = g(i, j) | \theta, 0 \leq i \leq N_{gl}, 0 \leq j \leq rl_{max} \quad (1)$$

where j is the number of elements, i is the intensity in the direction θ , N_{gl} is the maximum gl , and rl_{max} is the maximum length. We calculated 11 texture feature descriptors, which are short run emphasis (SRE), long run emphasis (LRE), short run low gray-level emphasis (SRLGLE), short run high gray-level emphasis (SRHGLE), long run low gray-level emphasis (LRLGLE), long run high gray-level emphasis (LRHGLE), run percentage (RP), low gray-level run emphasis (LGLRE), high gray-level run emphasis (HGLRE), run length non-uniformity normalized (RLNN), and run length non-uniformity (RLN) [36].

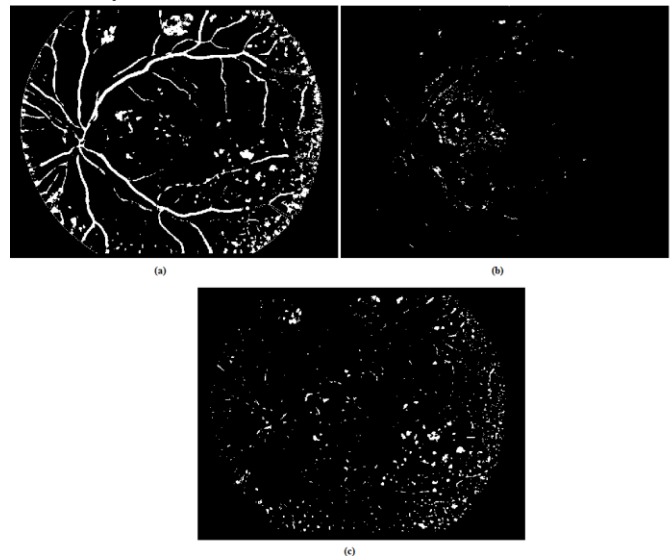


Fig 3. Segmentation Result (a) BV (b) EX (c) MA and HEM

C. SEGMENTATION

In this subsection, we first give a brief illustration of the CNN identifications and operations. Then, we demonstrate in detail the U-Net architecture and its hyperparameters that are changed to improve training and validation accuracy. The segmentation phase by the U-Net model positively affects the classification of the four DR grades (mild NPDR, moderate NPDR, severe NPDR, and PDR). In addition, it is considered a universal method to extract the four pathological changes by training the model on each sign's GTs. Fig 2 shows the segmentation phase result

1) GRADIENT WEIGHTING

We compute multi-scale multi-orientation weights for each pixel in a normalized image I_N based on the gradient magnitude at that pixel. The gradient magnitude values for different scales (σ_G) and different orientation (θ_G) are obtained by the convolution of the normalized image with the rotated first order derivative of the Gaussian kernel:

$$I_M(x, y, \sigma_G, \theta_G) = \left[\left(\frac{\partial G(x, y, \sigma_G)}{\partial x} \Big|_{\theta_G} \otimes I_N(x, y) \right)^2 + \left(\frac{\partial G(x, y, \sigma_G)}{\partial y} \Big|_{\theta_G} \otimes I_N(x, y) \right)^2 \right]^{1/2} \quad (2)$$

where $\theta_G \in \{0, \pi/12, \dots, \pi/2\}$ denotes the rotation angle of the Gaussian derivative kernel and the Gaussian kernel is given by $G(x, y, \sigma_G) = (1/\sqrt{2\pi\sigma_G^2})e^{-((x^2 + y^2)/2\sigma_G^2)}$ where $\sigma_G \in \{1, 2, 3, 4, 5\}$ σ_G is the standard deviation of the Gaussian kernel which is used as scaling parameter.

The weight of a pixel is inversely related to the gradient values at the pixel location, so that for pixels with small gradient magnitude (smooth regions), the weight is large, and for pixels with large gradient magnitude (such as on the edges), the output weight is small. The gradient-weighted image is obtained by

$$I_W(x, y, \sigma_G, \theta_G) = \frac{1 - I_M(x, y, \sigma_G, \theta_G)^2}{1 + I_M(x, y, \sigma_G, \theta_G)^2} \quad (3)$$

The final multi-orientation gradient-weighted image I_{WO} is defined as the sum of the individual gradient-weighted images in all orientations for each scale separately via

$$I_{WO}(x, y, \sigma_G) = \sum_{\theta_G=0}^{\pi/2} I_W(x, y, \sigma, \theta_G) \quad (4)$$

The multi-orientation gradient-weighted images are used in the successive thresholding process to extract candidates. Examples of the obtained results are illustrated in the last row. To cover all microaneurysms sizes, the multiorientation gradient-weighted images are obtained at several scales. The final multi-orientation and multi-scale gradientweighted image I_{WOS} is obtained by the summation of I_{WO} over all selected scales

$$I_{WOS}(x, y) = \sum_{\sigma_G=1}^5 I_{WO}(x, y, \sigma_G) \quad (5)$$

2) U-NET ARCHITECTURE

It is a CNN model that is used to localize the abnormalities areas. If CNN is used to learn the image feature map to exploit new feature maps and convert the image to feature vector, the U-Net construct the image from this feature vector [42]. The U-Net architecture consists of three phases that make the architecture take the (U) shape, which are contraction (down), bottleneck (the middle bottom), and expansion (up). In each phase, we can increase or collapse the number of the blocks. In the utilized architecture, we added three blocks in the contraction stage after the input. Each block includes two CONV (3 × 3) layers with RELU activation and followed by one MP (2 × 2) layer. The number of kernels is duplicated after each block as we started with 32 kernels and increased to 512 kernels or feature maps in the bottleneck phase. After that, the architecture starts the expansion phase by doing the up-sampling CONV (2×2) and RELU activation. This phase consists of three blocks as well as the contraction blocks. Each block includes two CONV (3 × 3) with RELU activation and followed by up-sampling CONV (2 × 2). The kernels or feature maps number are reduced to the half after each block. Finally, one CONV (1×1) is added to result in the segmentation maps. We trained the architecture four times on the BV, EX, MA, and HM GTs and predicted four segmenting images from each input.

We trained and evaluated the model by 10-fold cross-validation with 30 epochs and 100 steps for each epoch. In prediction, the batch size was 16, stride (2, 2) for concatenation, “same” padding, and dropout equals (0.1). We optimized the model by Adam optimizer with the learning rate (lr) equals to $1e - 3$. Finally, we utilized a sigmoid function and binary-cross entropy. The utilized U-Net architecture is shown in Algorithm 2. C is convolution, U is upsampling, 2@ is two consecutive convolutions, 1@ ConvT is one convolution transpose, plus (+) is a concatenation of the output of 1 convT layer of the expansion, and the feature maps of the contraction in the same level.

After segmenting EX, BV, HM, and MA, we validated the results due to six performance measures, as illustrated in detail in the next section. In addition, we compare the resulting segmentation of the proposed ML-CAD system with the universal customized DL segmentation model with other current segmentation methods.

D. FEATURE EXTRACTION AND SELECTION

We applied this phase by utilizing conventional hand-crafted methods. The reason is that we need to complete the four lesion segmentation process we made. We segmented each disease sign to diagnose it in its early and advanced grades carefully. Therefore, we cared about appearing even small MA that formulates the early mild grade for the ocular specialist or physician. It is crucial to extract features from these small signs. The thing that needs more auditing and supervising, while other systems, such as Lam et al. [43], could not diagnose the mild grade by using CNN.

For BV images, we utilized GLCM to extract 12 different feature descriptors, as proposed by Gadkari [44]. The GLCM describes the texture features. GLCM computes the frequency of appearance of pixel pairs with specified values in a spatial relation in the processed image. We skeletonize the BV network. Then, we determine BP with red marks and dismiss dummy, terminal branches and points.

Meanwhile, we calculated the BV, MA, EX, and HM areas. There are four fields recorded in the feature vector. The feature vector consists of 12 GLCM descriptors, 4 ROIs areas, and BP count for each DR image. We applied PCA technique. It is utilized to describe the extracted features with low dimensional space without information loss [45] by defining the most correlated values.

E) Classification

In the proposed algorithm, a multilayer neural network with back propagation is employed for classification.

1) Architecture of artificial neural network

The size of input layer is equal to that of the input feature set. Each input is weighted with the appropriate weight. Sigmoid function is used as a transfer function as it gives output in the range of 0 and 1.

$$\text{sigmoid} = \frac{1}{1 + f^{-\sum(v_i w_{ij}) + b}} \quad (6)$$

where v_i refers to i th input, w_{ij} is the weight factor for the j th node, b is the bias and f is actually the activation function.

2) Network training

Training and learning functions are mathematical procedures used to automatically adjust the network's weights and biases to optimise the network performance. The network performance is measured by the average of the squared error (mse) between the network outputs and the targets.

$$\text{mse} = \frac{1}{L} \sum_{i=1}^L (C_i - O_i)^2 \quad (7)$$

where C_i represents the target class and O_i represents the actual output. The error is propagated back towards the hidden layer. The next step is to update the weights and biases using the error derivatives. In this experiment, 817 training samples have been used to train the network for 14 classes. Initially the weights were set to some random values. The training set consists of N data pairs (v_i, C) as where v_i refers the input and C is the corresponding target class. The weights are updated after each training cycle in order to minimise the overall network error. The training of the network continues until the overall error has crossed the threshold (105) level or fixed number of iterations (e.g 1000) has been completed.6

V RESULT AND DISCUSSION

PERFORMANCE METRICS

We utilized six different measures to evaluate the performance of the proposed ML-CAD system, i.e., SEN, specificity (SPE), DSC, accuracy (ACC), positive predictive value (PPV), and area under the curve (AUC), which are listed in Eqs. SEN is the rate of true positive (TP). SPE is the proportion of the true negatives (TN). The technique may be accurate without being sensitive, or it may be sensible without being specific. ACC is the ratio of true results, either TP or TN overall images. False positive (FP) is the ratio of false predictive or incorrect positive predictions. False negative (FN) is the ratio of incorrect negative predictions. DSC measures the resemblance between the predictions and GT. PPV is the proportion of the correct positive predictions over the correct and incorrect positive predictions. Finally, AUC is nearly half of the summing of the SEN and SPE.

$$\text{SEN/RE} = \frac{TP}{TP + FN} \quad (8)$$

$$\text{SPE} = \frac{TN}{TN + FP} \quad (9)$$

$$\text{DSC} = \frac{2 \times TP}{2 \times TP + FP + FN} \quad (10)$$

$$\text{ACC} = \frac{TP + TN}{TP + TN + FP + FN} \quad (11)$$

$$\text{PPV} = \frac{TP}{TP + FP} \quad (12)$$

$$\text{AUC} \approx 0.5 (\text{SEN} + \text{SPE})$$

TABLE 1. The comparison between the proposed ML-CAD system and others.

Method	ACC(%)	AUC(%)	SEN(%)	SPE(%)	PPV(%)	DSC(%)
CC[68]	89.2	85.20	72.4	83.4	72.6	74.2
ML-KNN[66]	72.1	74.9	67.7	82.2	68.4	75.3
ML-CAD	95.05	91.85	86.11	85.8	87.4	81.2
Proposed	96.3	93.46	89.23	87.04	90.12	88.56

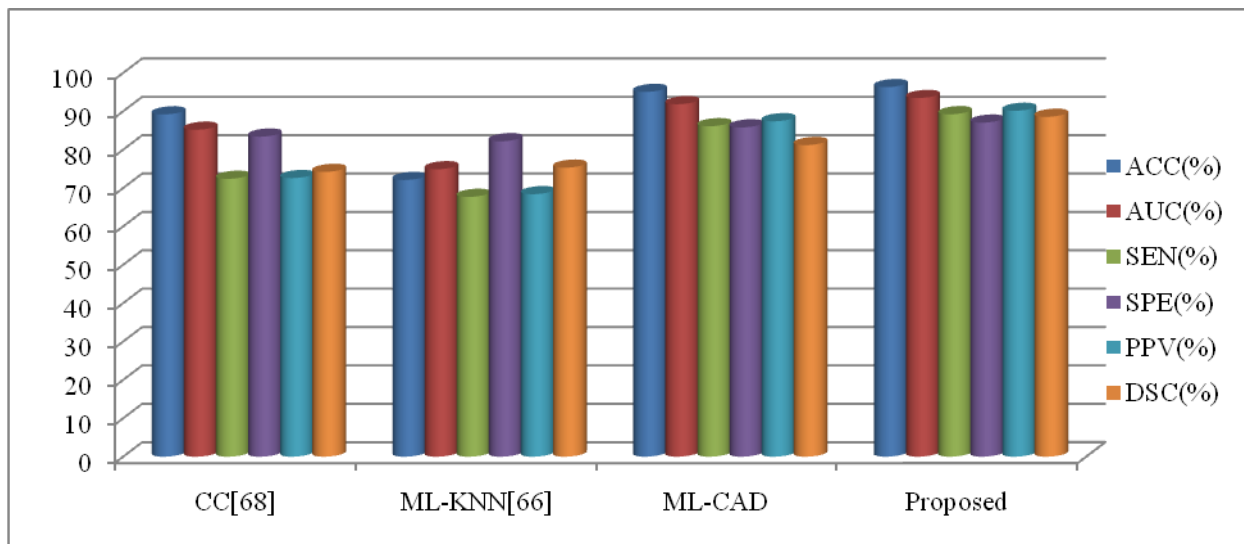


FIGURE 11. The comparison between the seven ML classifiers, abdelmaksoud et al., and the proposed ML-CAD system due to the six measures (ACC, AUC, SEN, SPE, PPV, and DSC).

V1 CONCLUSION AND FUTURE WORK

We developed a novel ML-CAD system that can be applied on varied datasets to diagnose diabetic retinopathy grades. At first, the proposed system filters and enhances the contrast. Then, it utilizes 11 texture feature descriptors by using GLRLM to determine the normal and DR images. Then, prepares the DR images by postprocessing steps for U-Net model. The multi-oriented gradient weighting is combined with U-Net model U-Net model to segment hemorrhages, exudates, Blood Vessels, and microaneurysms. The system extracts 6 features; 2 for BV using GLCM with 11 descriptors and bifurcation point’s count, 4 ROIs areas computations. Then, the system utilized the MLSVM for ML classification depending on the problem transformation. Finally, we computed 6 performance matrices averages of the proposed ML-CAD system. Our system proved that it is reliable and robust. It can be applied on the real world as it can be applied

on different color fundus images with different cameras’ settings, and different patients.

V11 REFERENCES

[1] World Health Organization, Diabetes. Accessed: Dec. 4, 2020. [Online]. Available: https://www.who.int/health-topics/diabetes#tab=tab_1

[2] L. Pizzarello, A. Abiose, T. Ffytche, R. Duerksen, R. Thulasiraj, H. Taylor, H. Faal, G. Rao, I. Kocur, and S. Resnikoff, “Vision 2020: The right to sight: A global initiative to eliminate avoidable blindness,” Arch. Ophthalmol., vol. 122, no. 4, pp. 615–620, 2004.

[3] T. Y. Wong and C. Sabanayagam, “Strategies to tackle the global burden of diabetic retinopathy: From epidemiology to

- artificial intelligence,” *Ophthalmologica*, vol. 243, no. 1, pp. 9–20, 2020.
- [4] N. Congdon, Y. Zheng, and M. He, “The worldwide epidemic of diabetic retinopathy,” *Indian J. Ophthalmol.*, vol. 60, no. 5, p. 428, 2012.
- [5] Z. Li, S. Keel, C. Liu, Y. He, W. Meng, J. Scheetz, P. Y. Lee, J. Shaw, D. Ting, T. Y. Wong, H. Taylor, R. Chang, and M. He, “An automated grading system for detection of vision-threatening referable diabetic retinopathy on the basis of color fundus photographs,” *Diabetes Care*, vol. 41, no. 12, pp. 2509–2516, Dec. 2018.
- [6] T. Hassan, M. U. Akram, B. Hassan, A. Nasim, and S. A. Bazaz, “Review of OCT and fundus images for detection of macular edema,” in *Proc. IEEE Int. Conf. Imag. Syst. Techn. (IST)*, Sep. 2015, pp. 1–4.
- [7] M. U. Saeed and J. D. Oleszczuk, “Advances in retinal imaging modalities: Challenges and opportunities,” *World J. Ophthalmol.*, vol. 6, no. 2, pp. 10–19, 2016.
- [8] V. Gulshan, L. Peng, M. Coram, M. C. Stumpe, D. Wu, A. Narayanaswamy, S. Venugopalan, K. Widner, T. Madams, J. Cuadros, R. Kim, R. Raman, P. C. Nelson, J. L. Mega, and D. R. Webster, “Development and validation of a deep learning algorithm for detection of diabetic retinopathy in retinal fundus photographs,” *J. Amer. Med. Assoc.*, vol. 316, no. 22, pp. 2402–2410, 2016.
- [9] S. El-Sappagh, T. Abuhmed, S. M. R. Islam, and K. S. Kwak, “Multimodal multitask deep learning model for Alzheimer’s disease progression detection based on time series data,” *Neurocomputing*, vol. 412, pp. 197–215, Oct. 2020.
- [10] S. El-Sappagh, T. Abuhmed, and K. S. Kwak, “Alzheimer disease prediction model based on decision fusion of CNN-BiLSTM deep neural networks,” in *Intelligent Systems and Applications*, K. Arai, S. Kapoor, and R. Bhatia, Eds. Cham, Switzerland: Springer, 2020, pp. 482–492.
- [11] G. Lim, V. Bellemo, Y. Xie, X. Q. Lee, M. Y. T. Yip, and D. S. W. Ting, “Different fundus imaging modalities and technical factors in AI screening for diabetic retinopathy: A review,” *Eye Vis.*, vol. 7, no. 1, pp. 1–13, Dec. 2020.
- [12] T. Abuhmed, S. El-Sappagh, and J. M. Alonso, “Robust hybrid deep learning models for Alzheimer’s progression detection,” *Knowl.-Based Syst.*, vol. 213, Feb. 2021, Art. no. 106688.
- [13] K. Y. Tey, K. Teo, A. C. Tan, K. Devarajan, B. Tan, J. Tan, L. Schmetterer, and M. Ang, “Optical coherence tomography angiography in diabetic retinopathy: A review of current applications,” *Eye Vis.*, vol. 6, no. 1, pp. 1–10, 2019.
- [14] S. M. S. Islam, M. M. Hasan, and S. Abdullah, “Deep learning based early detection and grading of diabetic retinopathy using retinal fundus images,” 2018, arXiv:1812.10595. [Online]. Available: <http://arxiv.org/abs/1812.10595>
- [15] A. C. Tan, G. S. Tan, A. K. Denniston, P. A. Keane, M. Ang, D. Milea, U. Chakravarthy, and C. M. G. Cheung, “An overview of the clinical applications of optical coherence tomography angiography,” *Eye*, vol. 32, no. 2, pp. 262–286, 2018.
- [16] A. Biran, P. S. Bidari, and K. Raahemifar, “Automatic method for exudates and hemorrhages detection from fundus retinal images,” *Int. J. Comput. Inf. Eng.*, vol. 10, no. 9, pp. 1599–1602, 2016.
- [17] G. L. Atlas and K. Parasuraman, “Detection of retinal hemorrhage from fundus images using ANFIS classifier and MRG segmentation,” *Biomed. Res.*, vol. 29, no. 7, pp. 1489–1497, 2018.
- [18] J. I. Orlando, E. Prokofyeva, and M. B. Blaschko, “A discriminatively trained fully connected conditional random field model for blood vessel segmentation in fundus images,” *IEEE Trans. Biomed. Eng.*, vol. 64, no. 1, pp. 16–27, Jan. 2017.
- [19] M. K. Fadafen, N. Mehrshad, and S. M. Razavi, “Detection of diabetic retinopathy using computational model of human visual system,” *Biomed. Res.*, vol. 29, no. 9, pp. 1956–1960, 2018.
- [20] D. W. Safitri and D. Juniati, “Classification of diabetic retinopathy using fractal dimension analysis of eye fundus image,” *AIP Conf.*, vol. 1867, Aug. 2017, Art. no. 020011.
- [21] E. AbdelMaksoud, S. Barakat, and M. Elmogy, “A comprehensive diagnosis system for early signs and different diabetic retinopathy grades using fundus retinal images based on pathological changes detection,” *Comput. Biol. Med.*, vol. 126, Nov. 2020, Art. no. 104039.
- [22] M. D. Abramoff, Y. Lou, A. Erginay, W. Clarida, R. Amelon, J. C. Folk, and M. Niemeijer, “Improved automated detection of diabetic retinopathy on a publicly available dataset through integration of deep learning,” *Invest. Ophthalmol. Vis. Sci.*, vol. 57, no. 13, pp. 5200–5206, 2016.
- [23] V. Bellemo, Z. W. Lim, G. Lim, Q. D. Nguyen, Y. Xie, M. Y. Yip, H. Hamzah, J. Ho, X. Q. Lee, W. Hsu, M. L. Lee, L. Musonda, M. Chandran, G. Chipalo-Mutati, M. Muma, G. S. W. Tan, S. Sivaprasad, G. Menon, T. Y. Wong, and D. S. W. Ting, “Artificial intelligence using deep learning to screen for referable and vision-threatening diabetic retinopathy in africa: A clinical validation study,” *Lancet Digit. Health*, vol. 1, no. 1, pp. e35–e44, 2019.
- [24] R. F. Mansour, “Deep-learning-based automatic computer-aided diagnosis system for diabetic retinopathy,” *Biomed. Eng. Lett.*, vol. 8, no. 1, pp. 41–57, Feb. 2018.
- [25] T. R. Gadekallu, N. Khare, S. Bhattacharya, S. Singh, P. K. R. Maddikunta, I.-H. Ra, and M. Alazab, “Early detection

- of diabetic retinopathy using PCA-firefly based deep learning model,” *Electronics*, vol. 9, no. 2, p. 274, Feb. 2020.
- [26] M. T. Hagos and S. Kant, “Transfer learning based detection of diabetic retinopathy from small dataset,” 2019, arXiv:1905.07203. [Online]. Available: <http://arxiv.org/abs/1905.07203>
- [27] B. Tymchenko, P. Marchenko, and D. Spodarets, “Deep learning approach to diabetic retinopathy detection,” 2020, arXiv:2003.02261. [Online]. Available: <http://arxiv.org/abs/2003.02261>
- [28] K. Xu, D. Feng, and H. Mi, “Deep convolutional neural network-based early automated detection of diabetic retinopathy using fundus image,” *Molecules*, vol. 22, no. 12, p. 2054, Nov. 2017.
- [29] H. Pratt, F. Coenen, D. M. Broadbent, S. P. Harding, and Y. Zheng, “Convolutional neural networks for diabetic retinopathy,” *Procedia Comput. Sci.*, vol. 90, pp. 200–205, Jan. 2016.
- [30] M. M. Butt, G. Latif, D. N. F. A. Iskandar, J. Alghazo, and A. H. Khan, “Multi-channel convolutions neural network based diabetic retinopathy detection from fundus images,” *Procedia Comput. Sci.*, vol. 163, pp. 283–291, Jan. 2019.
- [31] Y.-H. Li, N.-N. Yeh, S.-J. Chen, and Y.-C. Chung, “Computer-assisted diagnosis for diabetic retinopathy based on fundus images using deep convolutional neural network,” *Mobile Inf. Syst.*, vol. 2019, pp. 1–14, Jan. 2019.
- [32] M. A. Rahman, S. Liu, S. Lin, C. Wong, G. Jiang, and N. Kwok, “Image contrast enhancement for brightness preservation based on dynamic stretching,” *Int. J. Image Process.*, vol. 9, no. 4, p. 241, 2015.
- [33] E. Abdel-Maksoud, M. Elmogy, and R. Al-Awadi, “Brain tumor segmentation based on a hybrid clustering technique,” *Egyptian Informat. J.*, vol. 16, no. 1, pp. 71–81, Mar. 2015.
- [34] X. Tang, “Texture information in run-length matrices,” *IEEE Trans. Image Process.*, vol. 7, no. 11, pp. 1602–1609, Nov. 1998.
- [35] E. AbdelMaksoud, S. Barakat, and M. Elmogy, “A multi-label computeraided diagnoses system for detecting and diagnosing diabetic retinopathy,” in *Proc. 14th Int. Conf. Comput. Eng. Syst. (ICCES)*, Dec. 2019, pp. 373–386.
- [36] S. V. da Rocha, G. B. Junior, A. C. Silva, A. C. de Paiva, and M. Gattass, “Texture analysis of masses malignant in mammograms images using a combined approach of diversity index and local binary patterns distribution,” *Expert Syst. Appl.*, vol. 66, pp. 7–19, Dec. 2016